Available online at www.sciencedirect.com
ScienceDirect
Trans. Nonferrous Met. Soc. China 35(2025) 2969−2987
Transactions of Nonferrous Metals Society of China
www.tnmsc.cn

Effect of rolling direction and reduction on microstructure evolution and mechanical properties of Cu/1010 steel bimetal laminated composites

Bo PENG[1], Jia LIU[1], Hui-kun WANG[1], Xing-run SHAN[1], Guo-liang LI[1], Zi-di HANG[1], Jin-chuan JIE[1,2], Ting-ju LI[1,2]

1. Key Laboratory of Solidification Control and Digital Preparation Technology (Liaoning Province), School of Materials Science and Engineering, Dalian University of Technology, Dalian 116024, China;
2. Ningbo Institute of Dalian University of Technology, Ningbo 315000, China

Received 28 January 2024; accepted 23 October 2024

Abstract: The Cu/1010 steel bimetal laminated composites (BLCs) were rolled to different thicknesses to investigate the effect of rolling direction and reduction on the microstructure evolution and mechanical properties. The difference of mechanical properties between the Cu and 1010 steel causes different thickness reductions, percentage spread, and cladding ratios. The formation of strong texture induces larger strength of the rolled samples, and as the volume fraction of 1010 steel is larger in Route-A, its strength is consistently greater than that in Route-B. The obstruction of interface to crystal and dislocation slip results in the formation of interface distortion, inducing dislocation density gradient when the rolling reduction is low in Route-A. The slip planes of the Cu and 1010 steel are more prone to suffer the normal strain, while the shear strain of other crystal planes is obviously larger than the normal strain under rolling load near the interface.

Key words: Cu/steel bimetal laminated composite; rolling; microstructure evolution; mechanical properties; deformation behavior

1 Introduction

Bimetal laminated composites (BLCs) are widely used in industrial production since they usually have excellent properties beyond monometallic materials [1−3]. The Cu/steel BLCs can combine the high thermal and electric conductivity of Cu with the high strength and toughness of steel, and excellent overall performance can be accomplished [4,5]. Besides that, Cu−Pb/steel [6], tin bronze/steel [7] and aluminum bronze/steel [8] have been investigated by many researchers, and these BLCs are widely used in bearing, heat exchanger and transportation systems [9,10].

Various technologies have been developed to fabricate high-quality BLCs, such as vacuum diffusion bonding [11], explosive welding [12], casting and rolling bonding [13], hot press sintering [14] and centrifugal casting [15]. However, the BLCs prepared by single technology are immature for direct industrial production, thus the combination of various processes is necessary to enhance the interfacial bonding strength, refine the microstructure, and adjust the dimensions [16]. Rolling is commonly used in primary or secondary processing of BLCs to enhance the bonding strength and improve their mechanical properties [17]. The Cu/Al clad sheets were produced via the casting and rolling by MAO et al [18], and the interfacial microstructure, peel strength and crack propagation behavior were investigated by varying the annealing temperature. It is found that the thickness

Corresponding author: Jin-chuan JIE, Tel: +86-411-84708940, E-mail: jiejc@dlut.edu.cn
https://doi.org/10.1016/S1003-6326(25)66860-9
1003-6326/© 2025 The Nonferrous Metals Society of China. Published by Elsevier Ltd & Science Press
This is an open access article under the CC BY-NC-ND license (http://creativecommons.org/licenses/by-nc-nd/4.0/)

of intermetallic compound layer can be restricted up to 550 nm after annealing at 250 °C, and the Cu/Al clad sheet exhibits the maximal peel strength. LIU et al [19] used numerical simulation to study the rolling process of Mg/Al composite plates prepared by explosive welding, and it is found that 30% rolling reduction is the most effective for combination of the two components. The hetero-phase interface was investigated in Cu−Nb multilayer composites during the accumulative roll-bonding [20], and multiple dislocation−interface interaction mechanisms were proposed. The rolling process was also adopted on the preparation of Al/Cu/Al BLCs after explosive welding [21], and rolling enhanced their bonding strength by inducing the formation of wave interface.

The studies on rolling process of monometallic materials have been carried out extensively [22], and the variation of percentage spread, texture and anisotropy has been revealed by many researchers [23,24]. SUWAS et al [25] conducted the unidirectional rolling and cross rolling on Cu to reveal the texture evolution, and the results show that transitions from Cu to brass and S type texture were brought about by changing the rolling method. In-situ EBSD experiments were performed on dual phase steel by LI et al [26], and the microstructure evolution was investigated. The Taylor factor changes with the rolling deformation, and the fracture usually initiates from ferrite grains which are close to hard martensite grains. The Schmid factor of $\{111\}\langle uvw\rangle$ grain was thoroughly examined [27], and the results suggest that the regions with larger energy are more susceptible to deformation than the regions with lower energy.

The rolling deformation behavior of BLCs differs from that of monometallic materials due to their special macrostructure [28]. The presence of a heterogeneous interface affects crystal slip on both sides [29,30], inducing different microstructure evolution from that inside the layers. Texture analysis was conducted on the Cu−Nb multilayer composites after rolling process [31], and the specific β fiber in Cu and α fiber in Nb appear, which are different from their monometallic samples. The rolling deformation behavior and interface properties of Cu/Al BLCs fabricated by horizontal continuous casting were investigated by WANG et al [13], and it is found that suitable technology methods and parameters are the critical factors for obtaining defect-free interface. The isothermal deformation behaviors of the Cu/Al composites with and without a bonding interface were investigated [32]. The relative sliding between the Cu and Al layers occurred in Cu/Al composites lacking bonding interface, while for the Cu/Al composites with a bonding interface, the soft Al layer tends to flow in synchrony with the hard Cu layer due to the constraint effect of the interface.

Since the microstructure and interface bonding mechanisms of BLCs change after rolling, their mechanical properties become unpredictable [33]. It is widely known that the formation of textures and high-density dislocations can induce larger strength and lower plasticity [17]. WANG et al [34] studied the microstructure evolution and mechanical properties of Mo plates by cross rolling, and it is found that the presence of $\{001\}\langle 110\rangle$ texture increases the strength, but reduces the plasticity. Rolling was adopted on the 30CrMnSiNi2A ultrahigh strength steel, and about 50% increment in strength was obtained due to grain refinement and work hardening [24]. The interfacial structure and mechanical properties of Mg/Al composite plates were studied by ZHI et al [35], and the results show that the interface bonding strength and tensile strength increase simultaneously after thermal deformation due to the occurrence of recrystallization.

Cu/1010 steel BLC has high conductivity of Cu and high strength of 1010 steel, thus it is a reliable heat exchanger material. Rolling is a convenient method to obtain superior micro-structure and proper dimension. Although some results regarding the rolling process of BLCs have been obtained, there is currently limited research available on the rolling deformation behavior of BLCs with strong interfacial bonding. Therefore, two different rolling methods were adopted to reveal the mechanical response of the Cu and 1010 steel to rolling load. In this study, the rolling deformation behavior, microstructure evolution, and interface effect of Cu/1010 steel BLCs prepared by continuous solid/liquid bonding were investigated. Furthermore, the effect of diverse rolling directions and reductions on mechanical properties was revealed by hardness and tensile tests. The present study is of great significance for the investigation of bimetallic synergistic deformation behavior, and provides a research basis

for subsequent study of the rolling deformation of various BLCs.

2 Experimental

2.1 Sample preparation and microstructural characterization

The Cu/1010 steel BLCs were prepared by continuous solid/liquid bonding, and the detailed process methods were similar to those in Ref. [36]. The cold rolled 1010 steel (SAE 1010) was used, and the original microstructure was mainly composed of ferrite and pearlite. The raw material of Cu (99.9 wt.%) was melted in a graphite crucible by an electromagnetic induction heating furnace. The casting temperature was 1250 °C, and the cooling rate was 5−20 °C/s. The obtained Cu/1010 steel BLCs were milled to remove surface oxides, and cut to cuboids with dimensions of 6 mm × 6 mm × 30 mm, which contained the same thickness of both Cu and 1010 steel of 3 mm. The bonding strength of obtained Cu/1010 steel BLCs was tested in our previous research [37], which was above 160 MPa, and fracture occurred on the Cu side, indicating that the interfacial bonding strength was larger than that of the Cu side. The schematic diagram of sample preparation and rolling process is shown in Fig. 1, and the designation of the samples with different rolling directions and reductions is shown in Table 1. Two rolling directions were adopted: the Cu and 1010 steel were stacked through the rollers in Route-A; the Cu and 1010 steel were placed side by side through the rollers in Route-B. The synchronous rolling was carried out, and the rolling reduction in each step was 10% (0.6 mm) in both rolling methods. The rolling direction is named as RD, the direction perpendicular to the rolling surface is ND (normal direction), and the direction parallel to the surface and perpendicular to the rolling direction is TD (transversal direction), as shown in Fig. 1.

The microstructure of as-cast sample was observed using an optical metallographic microscope (OM, MEF−4A, Leica, Germany) and a transmission electron microscope (TEM, Model EM−002B, Topcon, Japan) equipped with an energy dispersive spectroscope (EDS). The grain size and texture were analyzed by electron backscattered diffraction (EBSD, Oxford Instruments Group, United Kingdom), and the step was 0.15 μm × 0.15 μm. The fracture surfaces of the rolled samples after tensile test were characterized using scanning electron microscope (SEM, Zeiss supra−55, Zeiss Corp., Germany). The samples for OM observation were prepared using standard metallographic methods. Samples were characterized after polishing and etched by the mixture of nitric acid and alcohol (4 vol.% HNO_3 and 96 vol.% ethanol) and $FeCl_3$ etching solution (5 vol.% HCl, 95 vol.% ethanol and 5 wt.% $FeCl_3$). EBSD analysis was performed after polishing the sample with argon ion polisher, the acceleration voltage was 20 kV, and the acquisition frequency was 37.7 Hz. The samples for TEM analysis were

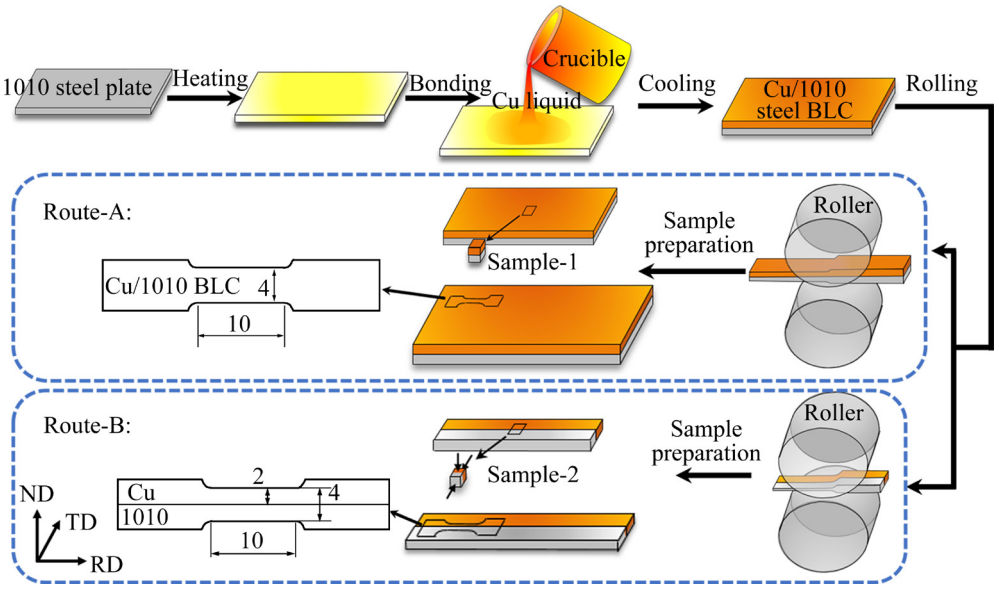

Fig. 1 Schematic illustration of Cu/1010 steel BLCs prepared by solid/liquid bonding and different rolling directions (unit: mm)

Table 1 Designations of different rolled Cu/1010 steel BLC samples

Route-A		Route-B	
Rolling reduction/%	Designation	Rolling reduction/%	Designation
10	A-10%	10	B-10%
30	A-30%	30	B-30%
50	A-50%	50	B-50%
70	A-70%	70	B-70%
90	A-90%	90	B-90%

prepared by focus ion beam (FIB, Helios G4 UX, Thermo Fisher, United States), and the lattice strain fields were calculated by the geometric phase analysis (GPA) method [38]. The morphology of fracture surface of the Cu/1010 steel BLCs was observed by laser scanning confocal microscopy (LSCM, OLS4000, Japan).

2.2 Mechanical tests

The samples for hardness test were obtained from the BLCs with different rolling reductions, and due to the anisotropy of the samples caused by rolling, the hardness of different surfaces was tested separately. The hardness was measured with a Vickers tester with a constant load of 300 g for 15 s, and at least eight testing points were carried out for each position to ensure the repeatability. Since the thickness of the samples changed after rolling, different numbers of test points were performed. The dimensions of tensile samples and preparation method are shown in Fig. 1. The quasi-static uniaxial tensile tests were performed by an electronic universal testing machine (UTM5105, Shenzhen Suns Aspect Technology Co., Ltd., China), and the strain rate was $5\times10^{-4}\ s^{-1}$. At least three tensile tests were performed for each sample to ensure repeatability, and the video extensometers and digital image correlation (DIC) techniques were employed to measure and calculate the strain fields, respectively.

3 Results

3.1 Microstructure evolution

The optical microstructure of the as-cast sample was observed, as shown in Fig. 2(a). Cu and 1010 steel are distinctly separated according to the different brightness and microstructure after etching.

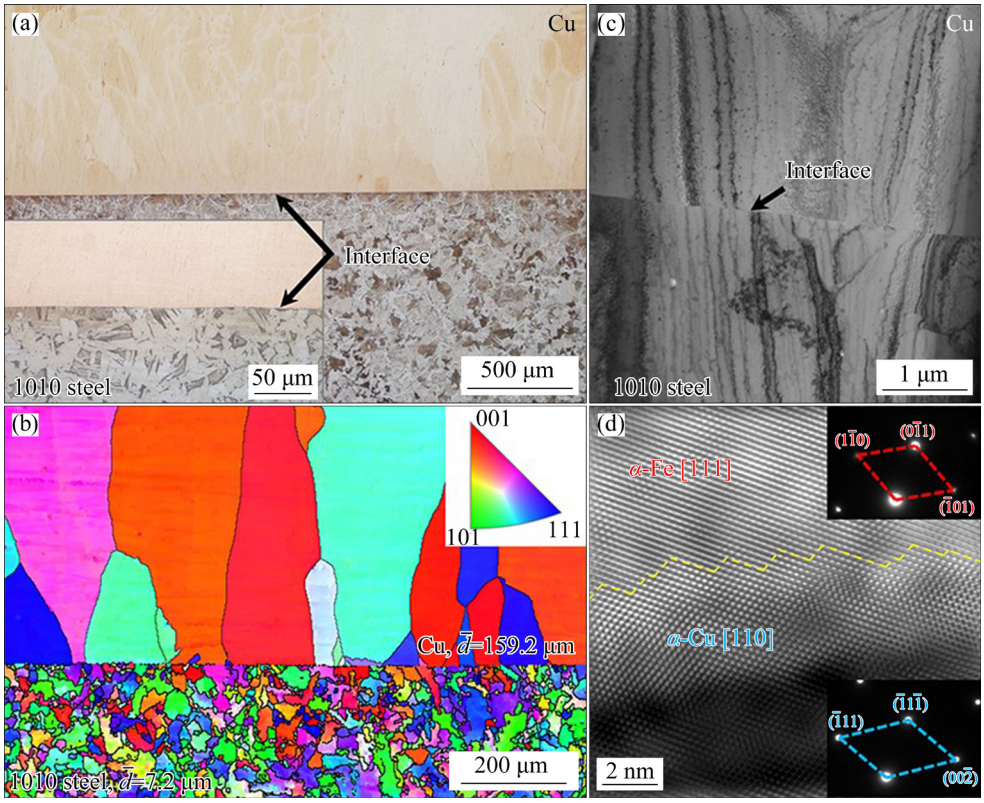

Fig. 2 Microstructure of as-cast Cu/1010 steel BLCs: (a) OM image; (b) IPF; (c) TEM image; (d) HRTEM image and corresponding SAED pattern

The 1010 steel mainly contains homogeneous ferrites and pearlite, and Cu is composed of single α-Cu. A flat interface is formed between Cu and 1010 steel, and the interface is well bonded without defects or discontinuous combination. The microstructure of the Cu/1010 steel BLC was observed by EBSD, and the invert pole figure (IPF) is shown in Fig. 2(b). The average grain size of Cu is approximately 159.2 μm, which is significantly larger than that of the 1010 steel (7.2 μm). More detailed characterization on the interface was carried out by TEM, and the results are shown in Figs. 2(c, d), where interatomic bonding is formed between the Cu and 1010 steel, ensuring sufficient interfacial bonding strength. Meanwhile, a parallel orientation relationship (OR) of $(0\bar{1}1)_{bcc\text{-}Fe}$ // $(\bar{1}1\bar{1})_{fcc\text{-}Cu}$ and $[111]_{bcc\text{-}Fe}$//$[110]_{fcc\text{-}Cu}$ is formed between Cu and Fe, which is always known as Kurdjumov−Sachs (K−S) OR. However, it is worth mentioning that not all of the interfaces have a defined OR, and more interfaces often exist in disordered forms, which has been reported in our previous study [39].

Figure 3 shows the OM images of the Cu/1010 steel BLCs with different rolling reductions and directions. The interface always remains well bonded without debonding or cracks during the two rolling processes. The original flat interface roughens after rolling, and the interfacial distortion becomes severe when the rolling reduction exceeds 30%. Figures 3(a_1−a_5) and (b_1−b_5) show interfacial microstructure evolution along the RD with increasing the rolling reduction from 10% to 90%. The elongation of grains is visible in the samples with larger rolling reductions, while this phenomenon is not found in Figs. 3(b_1−b_5). It is worth noting that the distortion of interface becomes intense with increasing the rolling reduction as shown in Figs. 3(c_1−c_5), and kinks of the interface induced by strong non-synergistic deformation appear in B-90% sample. In order to observe the anisotropy of the rolled samples, the

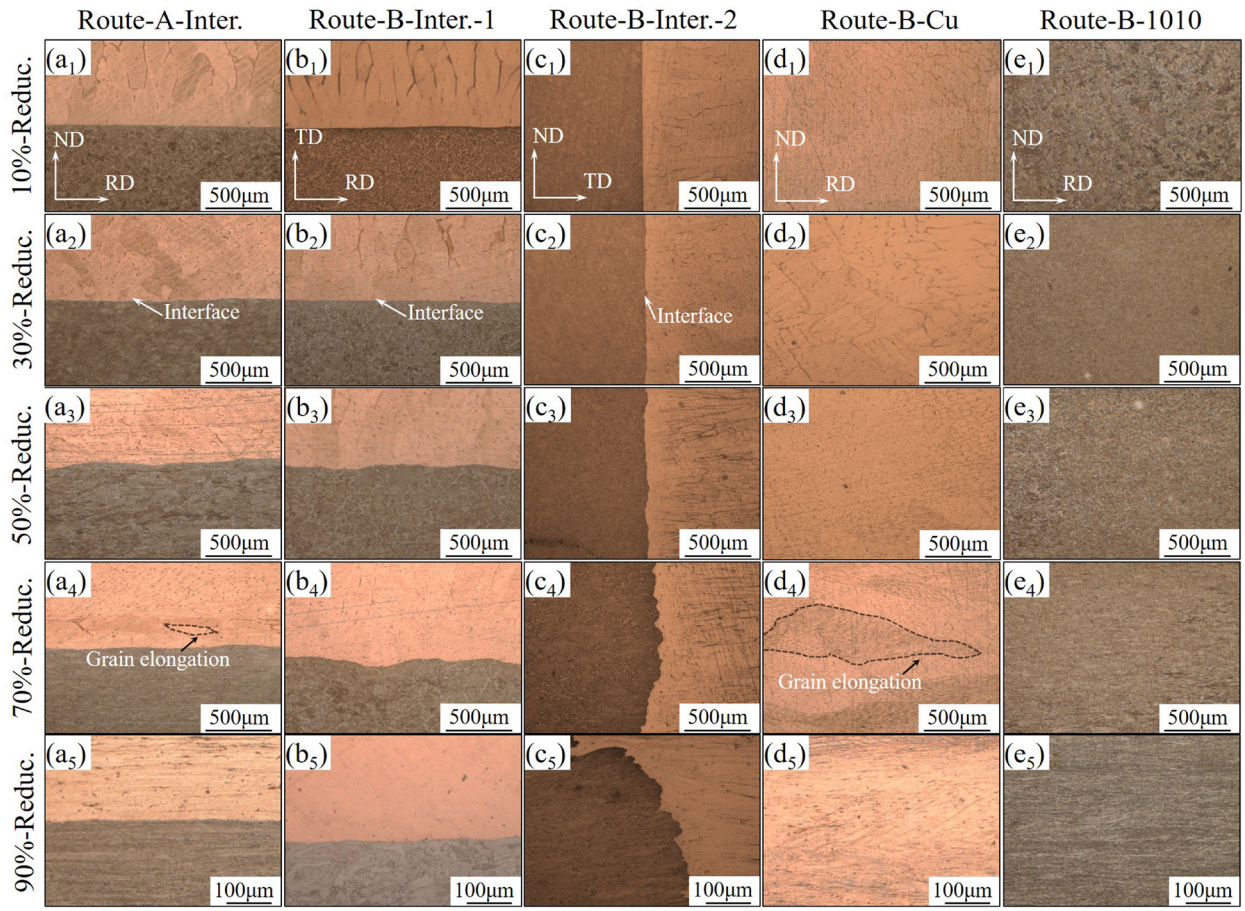

Fig. 3 OM images of Cu/1010 steel BLCs with different rolling reductions and directions: (a_1−a_5) Interfacial microstructure in Route-A; (b_1−b_5, c_1−c_5) Interfacial microstructure in Route-B; (d_1−d_5) Microstructure of Cu in Route-B; (e_1−e_5) Microstructure of 1010 steel in Route-B

OM images of Cu and 1010 steel in the RD−ND plane are shown in Figs. 3(d_1−d_5) and (e_1−e_5), respectively, in which the grain elongation is also visible. Although the OM results cannot visualize the microscopic details of the grains, it is still possible to observe some grains with significant deformation in the sample after 70% rolling reduction, which is more evident in the sample with 90% rolling reduction.

Significant slip bands can be found when the rolling reduction exceeds 50% according to the OM results, thus the samples of A-70% and A-90% were observed by EBSD as illustrated in Fig. 4. Figures 4(a, b) display the IPFs of A-70% and A-90% samples, respectively, and it is observed that the texture has been formed in A-70% sample, which becomes stronger in A-90% sample. The grain boundary angles of the two samples were calculated, as shown in Figs. 4(c, d), and the results show that Cu has lower grain boundary angle

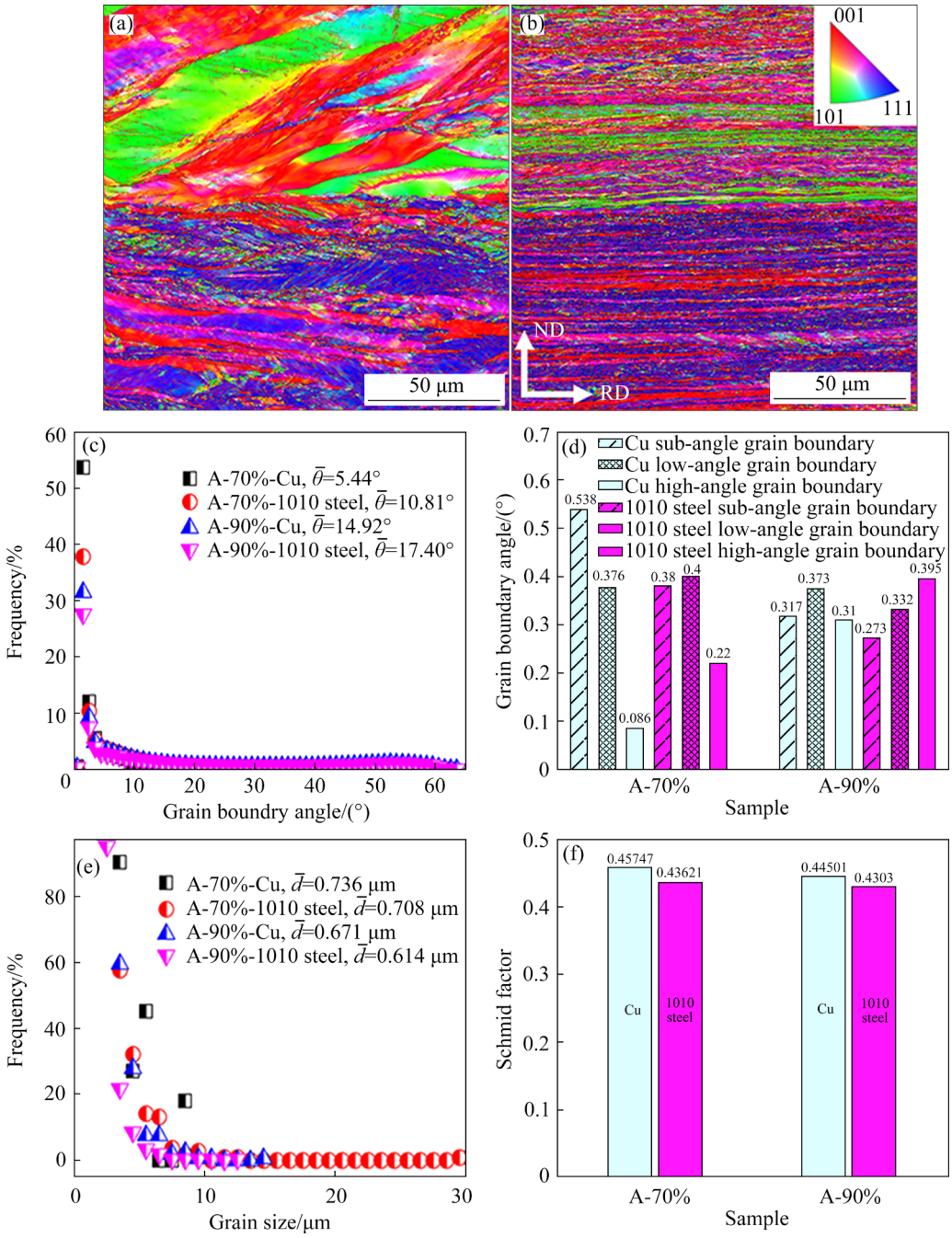

Fig. 4 IPFs of A-70% (a) and A-90% (b) samples, grain boundary angle distribution (c), grain boundary angle (d) (Sub-angle grain boundaries: 2°−5°, low-angle grain boundaries: 5°−15°, and high-angle grain boundaries: >15°), grain size distribution (e), and Schmid factor (f)

compared to the 1010 steel. Meanwhile, the grain boundary angles increase with increasing the rolling reduction, and the proportion of high-angle grain boundaries increases in the two components significantly. The grain size of the Cu and 1010 steel reduces after rolling as compared to that of the as-cast samples, and further decrease occurs when the rolling reduction increases from 70% to 90%, as shown in Fig. 4(e). The Schmid factor (m_s) is a crucial factor in the slip deformation, which is the sum of the tension along the RD and the compression along the ND for a cold rolled sample. Therefore, the Schmid factor can be calculated as follows [40]:

$$m_s=0.5(\cos\varphi_{RD}\cos\lambda_{RD}-\cos\varphi_{ND}\cos\lambda_{ND}) \quad (1)$$

where $\varphi_{(RD,ND)}$ is the angle between the direction normal to the slip plane and RD or ND, $\lambda_{(RD,ND)}$ is the angle between the slip direction and RD or ND. The m_s of 1010 steel is lower than that of Cu as illustrated in Fig. 4(f), indicating that the 1010 steel is more resistant to slip than Cu. The rolling process also increases the difficulty of slip deformation due to the reduced m_s.

In Route-B, since the texture of the two components in the ND−RD plane is similar to that in Route-A, Fig. 5 only shows the texture evolution of A-70% and A-90% samples. As strong texture is absent in the samples with lower rolling reductions, only the partial orientation distribution functions (ODFs) of A-70% and A-90% samples are presented in Figs. 5(a−h). The ODFs of Cu with 70% thickness reduction are primarily composed of Cube ({100}⟨001⟩) and α ({110}⟨110⟩) textures, which are uncommon in the deformed alloys, suggesting that the deformation of A-70% sample is insufficient. On the contrary, the cube texture is rare in Cu of A-90% sample, and strong β-fiber textures

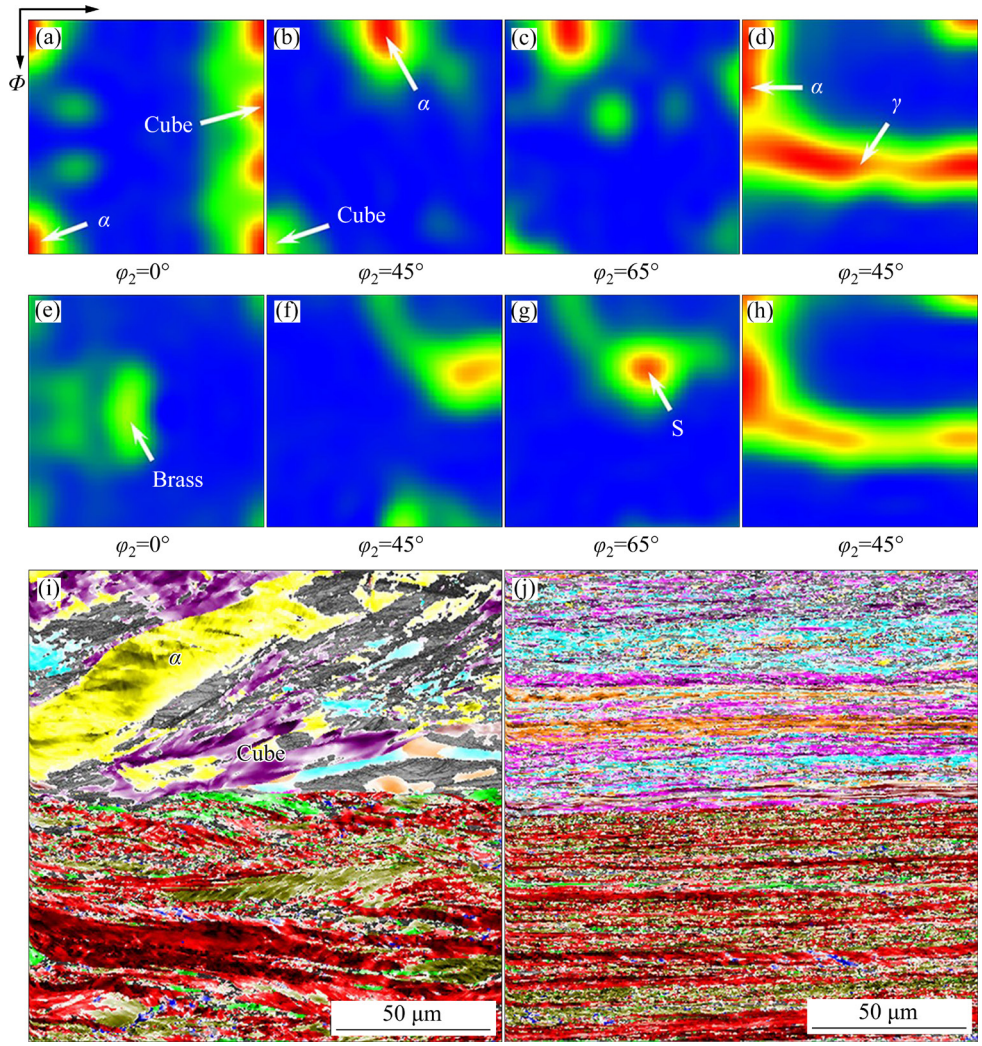

Fig. 5 ODFs of Cu in A-70% (a−c), 1010 steel in A-70% sample (d), Cu in A-90% sample (e−g), 1010 steel in A-90% sample (h), and special orientation distribution of A-70% (i) and A-90% (j) samples

composed of S ({123}⟨634⟩), Copper ({112}⟨111⟩), and Brass ({112}⟨111⟩) are formed. The 1010 steel samples with 70% and 90% thickness reduction all exhibit strong α (⟨110⟩//RD) and γ ({111}⟨112⟩) components, which are the major texture components in the rolled bcc metal.

In order to evaluate the texture distribution and influence of the interface during the rolling, specialized orientation distribution was calculated as shown in Figs. 5(i, j). Table 2 presents the major texture components of rolled fcc and bcc metals, along with the respective volume fractions in Cu and 1010 steel layers for A-70% and A-90% samples. The volume fraction of each component was calculated using a standard capture misorientation angle of 15°. The texture is not formed at some positions of A-70% sample, while A-90% sample is saturated with the texture as shown in Figs. 5(i, j). It is found that A-70% sample mainly comprises two types of texture, α and Cube, which are consist with the results of ODF. However, as the rolling reduction increases to 90%, the textures are almost dominated by Brass, S and Copper, and their distribution becomes more uniform. The 1010 steel exhibits stronger fiber textures in A-90% sample compared to those in A-70% sample, while their texture components are nearly identical. It is also found that all of the textures near the interface are similar to those inside the layers, suggesting that the interface does not play a significant role in the formation of texture.

Table 2 Selected major texture components of rolled fcc and bcc metals and corresponding volume fraction in rolled BLC samples

Material	Color	Component	{*hkl*}⟨*uvw*⟩	Volume fraction/%	
				A-70%	A-90%
Cu	Turquoise	S	{123}⟨634⟩	6.2	61.2
	Orange	Brass	{110}⟨112⟩	3.5	21.8
	Pink	Copper	{112}⟨111⟩	1.5	28.6
	Yellow	α	{110}⟨110⟩	20.6	0.6
	Purple	Cube	{100}⟨001⟩	22.4	6.22
1010 steel	Red	α	⟨110⟩//RD	72.6	70.6
	Blue	γ	⟨111⟩//TD	7.1	10.6
	Green	γ	⟨100⟩//TD	5.3	4.7
	Olive green	γ	{111}⟨112⟩	23.0	26.8

3.2 Mechanical behavior

The difference in mechanical properties and crystal structure of the Cu and 1010 steel results in distinct deformation behavior during the two rolling processes. Figure 6(a) shows the variation of thickness reduction and percentage spread of the Cu and 1010 steel, respectively. Both of the thickness reduction and percentage spread of Cu are larger than those of 1010 steel in the two rolling processes, indicating that Cu suffers severer deformation than 1010 steel. Figure 6(b) shows the cladding ratio (δ) of the Cu/1010 steel BLCs with different rolling reductions. The cladding ratio δ is calculated through dividing the total thickness of the Cu/1010 steel BLC by the thickness of Cu, as expressed as

$$\delta = \frac{H_{\mathrm{Cu}}}{H_{\mathrm{Total}}} \tag{2}$$

where H_{Cu} is the thickness of Cu, and H_{Total} is the total thickness of Cu/1010 steel BLC. As a result of severer deformation of Cu, the cladding ratio decreases in Route-A. Since strong texture has formed in the 1010 steel of A-70%, the deformation is difficult to occur. Therefore, the deformation is concentrated on the Cu side when the rolling reduction increases from 70% to 90%, resulting in a

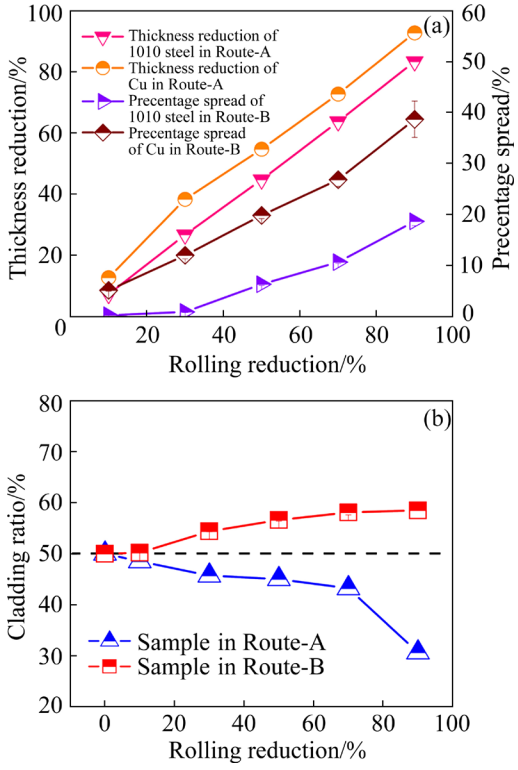

Fig. 6 Thickness reduction and percentage spread (a) and cladding ratio (b) of Cu/1010 steel BLCs after different rolling reductions and methods

sharp decrease in cladding ratio. Due to larger modulus and hardness of 1010 steel, greater rebound occurs after rolling deformation, resulting in lower plastic deformation of 1010 steel than that of Cu. In addition, different plastic flow characteristics of the Cu and 1010 steel along the RD and TD also induced slight bending of the samples as well as variations in cladding rate.

Figure 7 shows the Vickers hardness of the samples in the two rolling processes. The increase in the rolling reduction causes a corresponding increase in the hardness, and the hardness of 1010 steel is always larger than that of Cu, as shown in Figs. 7(a, b). The hardness of 1010 steel in B-10% sample is larger than that in A-10% sample due to the surface hardening. On the contract, the hardness of 1010 steel in Route-A is larger than that in Route-B when the rolling reduction exceeds 30%, which is believed that the texture has formed, and induced larger hardness. Due to larger deformation of Cu in Route-A, its hardness is greater than that in route-B in each rolling reduction. In order to eliminate the effect of surface hardening and texture, the average hardness in the plane of ND−RD in two routes was calculated and compared, as shown in Table 3. It is found that the hardness of samples in Route-A is larger than that in Route-B when the rolling reduction is less than 90%, suggesting that some other factors affect the hardness. The hardness of Cu is almost identical in A-90% and B-90% samples, while the hardness of 1010 steel is larger in B-90% sample than that in A-90% sample.

The engineering stress−strain curves of Cu/1010 steel BLCs in both as-cast and rolled forms are shown in Fig. 8(a). The rolled samples have larger yield strength (YS) compared to the as-cast sample, and as the rolling reduction increases, the YS further increases. The ultimate tensile strength (UTS) of A-10% and B-10% samples is essentially the same as that of the as-cast sample. Meanwhile, original strain hardening stage disappears, and the strength of the samples remains constant during uniform plastic deformation in A-10% and B-10% samples. The YS of the samples with the rolling reductions of 10% and 30% is approximately equal in two routes, while the YS of the samples rolled in Route-A is larger than that in Route-B when the rolling reduction is over 30%,

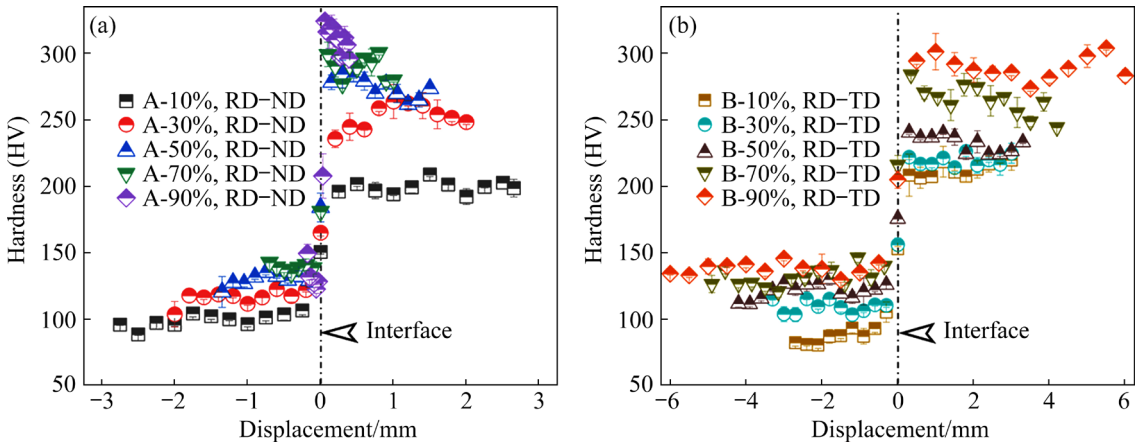

Fig. 7 Vickers hardness of Cu/1010 steel BLCs after different rolling reductions in RD−ND plane of Route-A (a) and in RD−TD plane of Route-B (b)

Table 3 Average hardness of BLCs after different rolling reductions in ND−RD plane (HV)

Rolling reduction/%	A-Cu	B-Cu	A-1010 steel	B-1010 steel
10	99.3±4.9	88.1±7.7	209.1±14.1	201.7±6.7
30	116.5±5.1	105.8±9.1	252.3±8.9	221.0±8.9
50	129.5±4.0	111.4±6.2	274.1±7.1	266.9±19.4
70	139.1±2.4	133.7±6.7	289.5±8.0	283.2±3.6
90	133.5±7.7	138.0±3.6	310.4±8.9	317.2±7.2

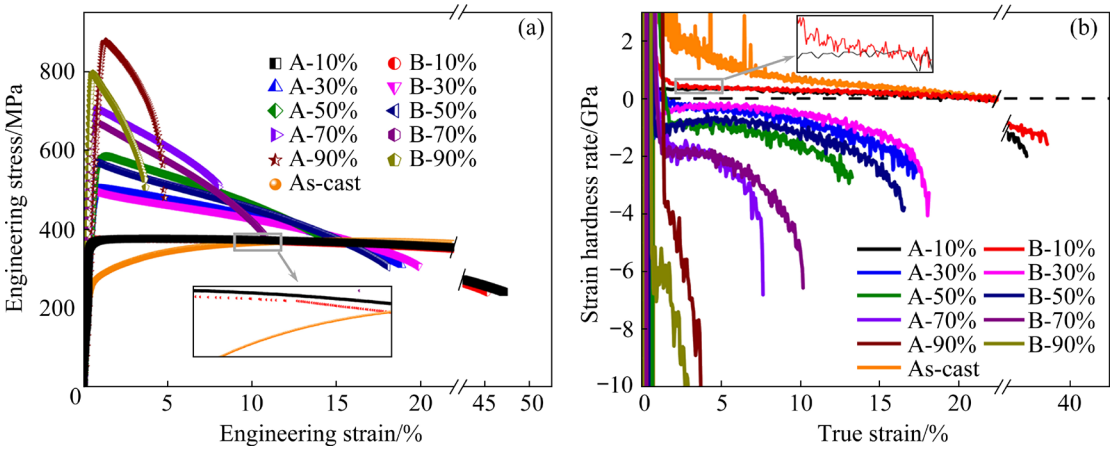

Fig. 8 Engineering stress−strain curves of Cu/1010 steel BLCs in as-cast, Route-A and Route-B (a), and corresponding strain hardness rate curves (b)

and this effect is the most significant at 90% reduction. The true strain and true stress are calculated as follows:

$$\varepsilon_{\text{true}}=\ln(1+\varepsilon_{\text{eng}}) \tag{3}$$

$$\sigma_{\text{true}}=(1+\varepsilon_{\text{eng}})\cdot\sigma_{\text{eng}} \tag{4}$$

where ε_{eng} and $\varepsilon_{\text{true}}$ are engineering strain and true strain, respectively, σ_{eng} and σ_{true} are engineering stress and true stress, respectively, and the strain hardness rate curves are obtained by differentiation of true stress to true strain as shown in Fig. 8(b) (the true stress−strain curves are not shown here). The samples of as-cast, A-10% and B-10% suffer a strain-hardening stage before the plastic instability, while other samples lose strain-hardening capacity, and the strength starts to decrease directly after yielding.

The tensile deformation behavior of Cu/1010 steel BLCs is more complex than that of homogenous materials due to their special macrostructure. Figures 9(a−d) present the strain distribution in the fracture regions of A-30%, B-30%, A-70% and B-70% samples, respectively. Both sides of A-30% are concave and the strain exhibits bimodal distribution along the TD as shown in Fig. 9(a). The bimodal distribution of the strain field in A-70% disappears, and the strain is distributed more uniformly along the TD (Fig. 9(c)). Due to different mechanical properties of Cu and 1010 steel, their deformation behaviors also show some difference even if they present in the same sample as shown in Figs. 9(b) and (d). Due to stronger deformability of Cu, the fracture concentrates in a broader region compared to the 1010 steel. The strain also exhibits bimodal distribution in Cu of A-30%, while the maximum strain in the 1010 steel concentrates in one region. Although the bimodal distribution of strain disappears in B-70%, the deformation of Cu is still over a larger area compared to that of the 1010 steel.

In order to investigate the deformation characteristics and fracture mechanisms of the Cu/1010 steel BLCs, the full width at half maxima (FWHM) of the strain distribution along different paths is counted and shown in Figs. 9(e) and (f). The FWHM of all the samples decreases with increasing the rolling reduction. The samples in Route-A show typical Orowan alternative slip fracture characteristics [41], where deformation mainly occurs at two intersecting slip bands, and the intersection suffers the largest concentrated deformation, leading to final fracture. In contrast, the significant and concentrated deformations are observed on the 1010 steel of the samples in Route-B, where the FWHM is the lowest as shown in Fig. 9(f), suggesting that the overall failure of BLCs is caused by the 1010 steel.

The fracture surfaces of A-10%, B-10%, A-50%, B-50%, A-90%, and B-90% samples are shown in Fig. 10. Due to their different morphologies, the interface between Cu and 1010 steel can be clearly distinguished by the yellow dashed line. It is found that the interfaces remain consistently well bonded after rolling and tensile fracture, with no occurrence of interfacial delamination or peeling. The samples with 10%- and 50%-rolling reductions suffer large plastic deformation before fracture,

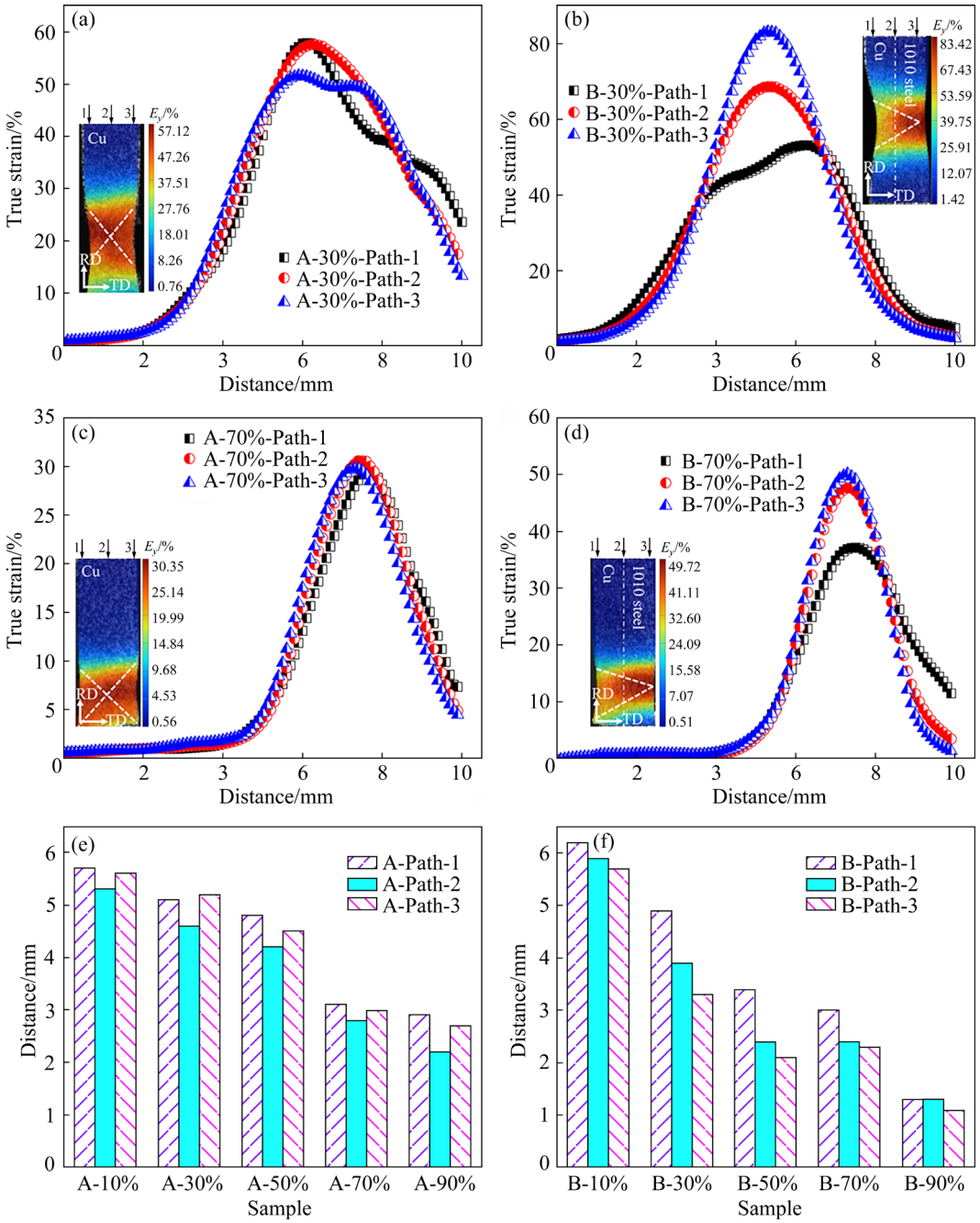

Fig. 9 True strain distribution along TD at tensile failure location of A-30% (a), B-30% (b), A-70% (c) and B-70% (d) samples, and FWHM of true strain−distance curves along different paths of samples in Route-A (e) and Route-B (f) (E_y is the strain along y direction)

resulting in numerous dimples on the fracture surface. Meanwhile, a dimple array appears on the interface as shown in Fig. 10(a), indicating that the heterogeneous interface induces the formation and development of dimples. Figures 10(e) and (f) show the fracture surfaces of A-90% and B-90% samples, respectively, and the corresponding LSCM images are shown in Figs. 10(g) and (h). Many dimples are formed on the fracture surface of Cu in A-90% sample, while the 1010 steel contains only a few of dimples. In addition, the inward depression of the interface suggests that the fracture of BLC is initiated by the interface and gradually propagates towards two sides. The fracture of Cu occurs after suffering significant local deformation due to its greater plastic deformation capacity. A kink is formed at the interface of B-90% sample, indicating that larger rolling reduction leads to severer deformation of the two materials and breakage through the obstruction effect of the heterogeneous

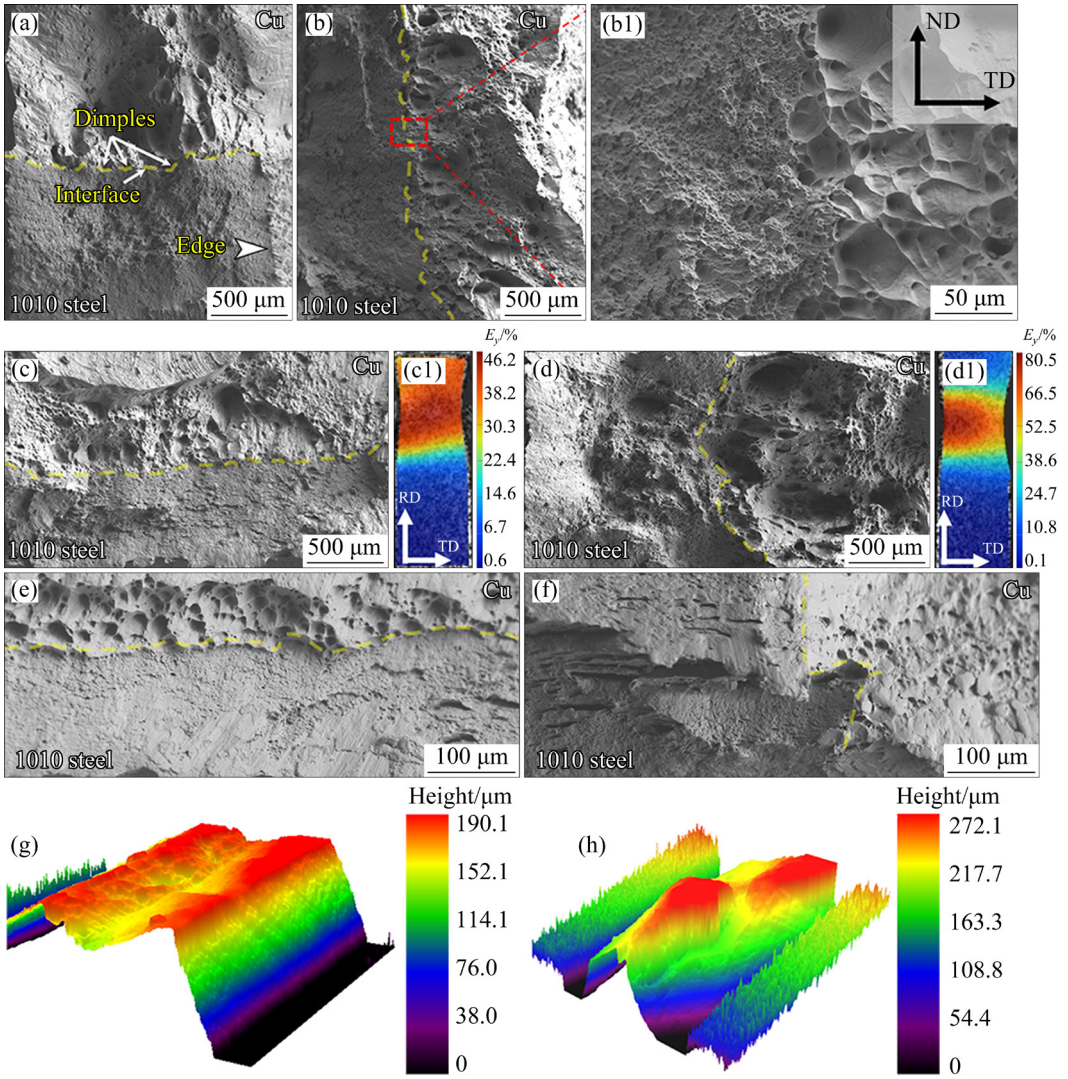

Fig. 10 Fracture surfaces of A-10% (a), B-10% (b), A-50% (c), B-50% (d), A-90% (e) and B-90% (f) samples; LSCM images of fracture surface of A-90% (g) and B-90% (h) samples; Partial enlarged image (b1) of marked area in (b); (c1, d1) Macro-strain fields

interface. Numerous dissociated ribs, shallow dimples, and uniform fracture surface height indicate that the Cu/1010 steel BLC fractures simultaneously.

4 Discussion

4.1 Obstruction effect of interface

In order to investigate microstructure evolution and the role of interface during rolling process, TEM tests were performed on B-90% sample, and the results are shown in Fig. 11. Figures 11(a−c) show the interfacial microstructure and corresponding elements distribution of Cu and Fe, in which the interface can be distinguished clearly. The original flat interface becomes distortion after rolling, while the interfacial transition zone or diffusion layer is not formed, and Cu and Fe are still well bonded. A number of slip bands parallel to the interface are formed on the 1010 steel side, and the grains of Cu also deform, while no directional slip bands are found, as shown in Figs. 11(a) and (d). Some dislocations tangle and pile-up are found in the grains near the interface as shown in Figs. 11(e−g), where the distortion of interface is severer than that of other positions, indicating that the motion of dislocations is obstructed by the interface, resulting in the distortion of interface. Meanwhile, some slip bands are not parallel to the interface, suggesting that the slip of crystals on both sides is impeded by the interface, which has been verified in samples prepared by rolling bonding [42].

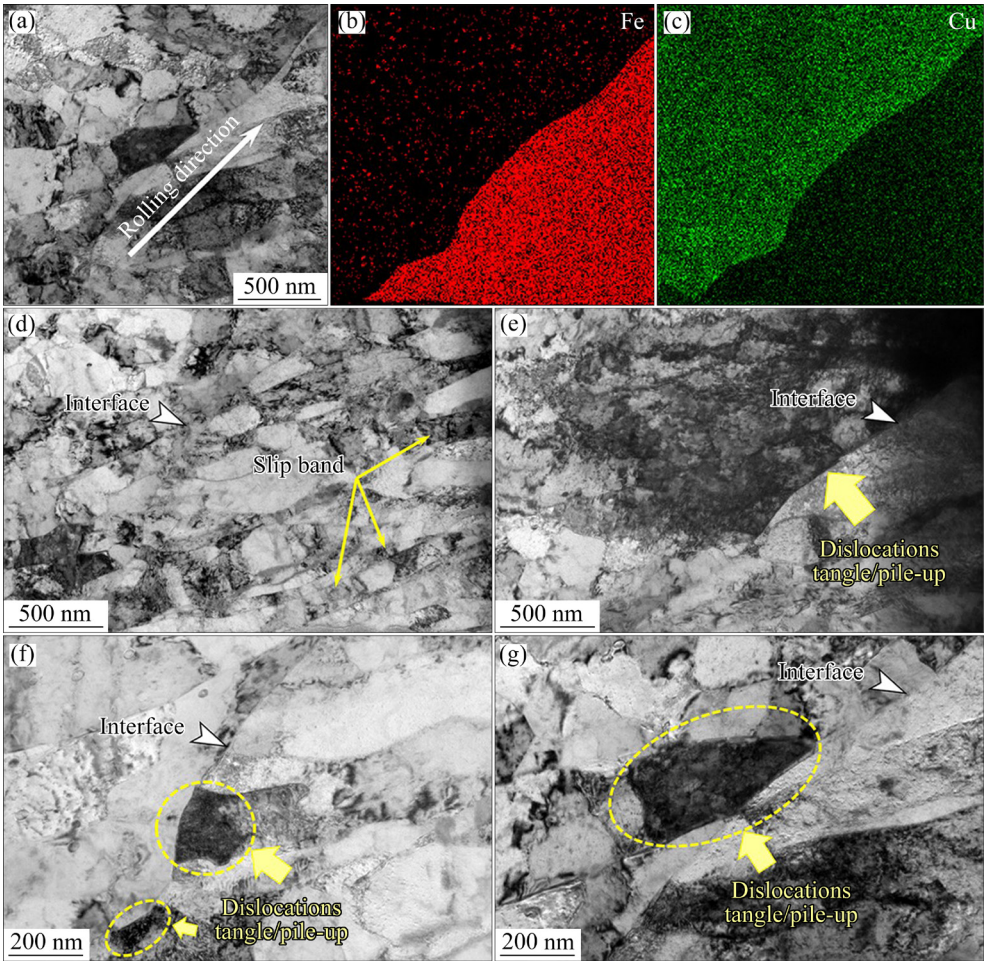

Fig. 11 Interfacial microstructure obtained by TEM for B-90% sample: (a−c) Interfacial microstructure and corresponding element distribution; (d−g) Detailed characterization of interface, dislocation and slip bands

More details of interfacial microstructure of B-90% sample were observed and analyzed by HRTEM with the assistance of GPA, and the results are shown in Fig. 12. Figure 12(a) shows a typical interface with K−S OR of $(1\bar{1}1)_{Cu}//(110)_{Fe}$. Since the zone axis of Fe is not parallel to that of the Cu, other crystal planes of the Fe cannot be distinguished. The image of selected region after inverse fast Fourier transform (IFFT) and filtering is shown in Fig. 12(b). The interface can be distinguished directly due to the difference in lattice structure between Cu and Fe, and the interfacial distortion still exits. The lattice strain fields were calculated, Figs. 12(c) and (f) show the IFFT images along the $(1\bar{1}1)_{Cu}//(110)_{Fe}$ and $(200)_{Cu}$, and Figs. 12(d) and (e), and (g) and (h) show the corresponding shear strain and normal strain fields, respectively. It is worth noting that since no crystal planes are parallel to the $(200)_{Cu}$ in Fe, the strain fields covered by triangles are false at the right bottom corner in Figs. 12(g) and (h). The directivity of shear strain is found along the $(1\bar{1}1)_{Cu}//(110)_{Fe}$ and $(200)_{Cu}$ as shown in Figs. 12(d) and (g), respectively, and the strain fields are not parallel to the interface due to the distortion of the interface. Since $(1\bar{1}1)$ and (110) are slip planes of Cu and Fe respectively, larger normal strain appears along the $(1\bar{1}1)_{Cu}//(110)_{Fe}$ than shear strain as shown in Figs. 12(d) and (e). In contrast, since $(200)_{Cu}$ is not slip plane of Cu, normal strain is difficult to occur, resulting in that shear strain is larger than the normal strain, as shown in Figs. 12(g) and (h). The slip deformation of Fe is much more difficult due to larger strength, resulting in that the shear and normal strain fields are all lower than those of Cu, as shown in Figs. 12(d) and (e).

The Cu/1010 steel BLCs rolled by different methods present different deformation behaviors due to the influence of the interface, leading to different mechanical properties and fracture modes. In order to observe deformation characteristics of the Cu/1010 steel BLCs after rolling, the microscopic

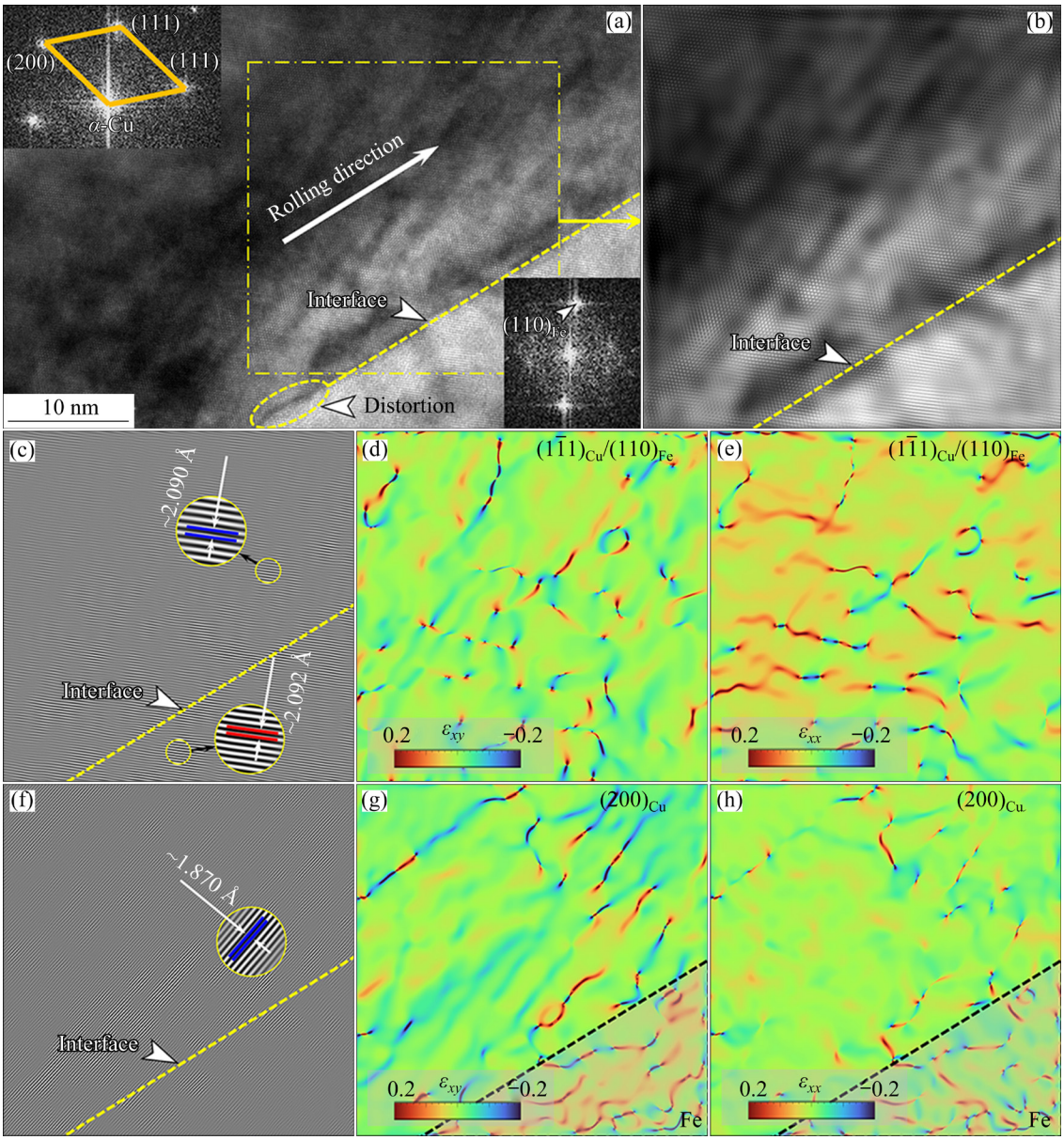

Fig. 12 Interfacial microstructure and corresponding strain field of B-90% sample: (a) HRTEM image of B-90%; (b) IFFT fringe for selected area; IFFT fringe along $(1\bar{1}1)_{Cu}//(110)_{Fe}$ after filtering (c) and corresponding strain field images of shear strain (d) and normal strain (e); IFFT fringe along $(200)_{Cu}$ after filtering (f) and corresponding strain field images of shear strain (g) and normal strain (h)

strain and kernal average misorientation (KAM) images of A-70% and A-90% samples are shown in Fig. 13. The large deformation regions are formed near the interface in A-70% sample, as shown in Fig. 13(a), and the strain gradually decreases towards the inner layers. A similar tendency is also found in KAM image as shown in Fig. 13(b), and the corresponding average KAM statistics is shown in Fig. 13(c). The whole KAM image was divided into 20 regions uniformly, and the average KAM was counted in each region as shown in Figs. 13(g1) and (g2). It is found that a dislocation density gradient is formed on the two sides of A-70%, i.e., the dislocation density is the largest near the interface and gradually decreases towards the layer, suggesting that the interface hinders crystal slip and induces the dislocations pile-up. Similar microscopic strain and KAM images of A-90% are shown in Figs. 13(d) and (f), respectively. Non-uniform strain zones still appear in the sample, while both of the strain and dislocation density no longer exhibit gradient distribution. As the rolling reduction increases from 70% to 90%, large-scale slip of the two layers causes further movement of

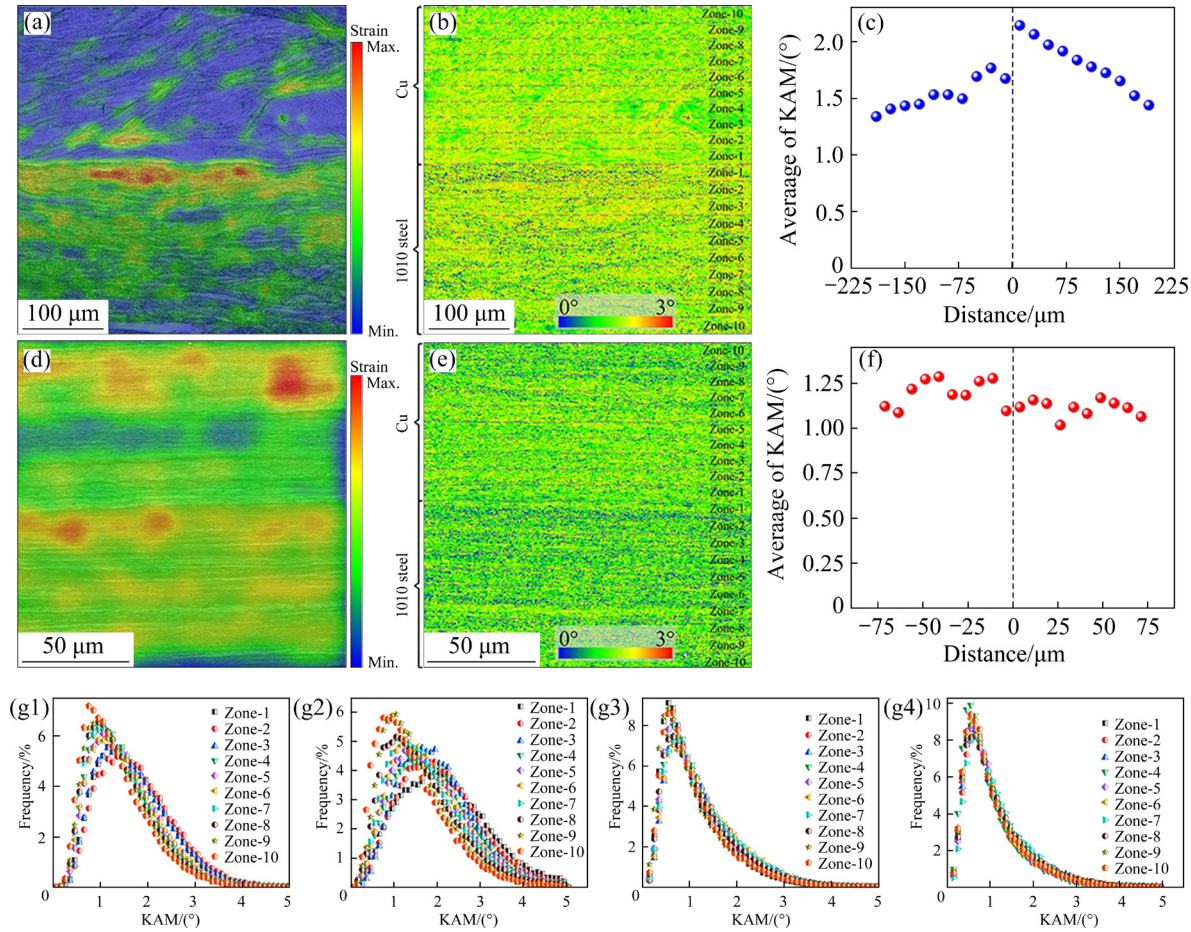

Fig. 13 Micro-strain maps from EBSD measurement of A-70% (a) and A-90% (d) samples; KAM maps of A-70% (b) and A-90% (e) samples; Averaged KAM values of A-70% (c) and A-90% (f) samples; KAM distribution in each zone of A-70%-Cu (g1), A-70%-1010 (g2), A-90%-Cu (g3), and A-90%-1010 (g4) samples

the interface, relaxing the original dislocations pile-up at the interface. Therefore, the interface has the strong obstruction effect on the crystal slip when rolling reduction is low, resulting in large number of dislocations pile-up; while the interface starts to slip and dislocations pile-up no longer occurs when the rolling reduction is increased to 90%. Other studies have reported that interface slip can only occur if the force acting on the interface is larger than its critical activation stress [43,44]. Therefore, sufficient rolling force is an important reason to induce large-scale slip of the interface and reduce dislocations tangle and pile-up.

4.2 Rolling and tensile deformation behavior

The entire process of the rolling deformation and tensile fracture of the Cu/1010 steel BLCs is illustrated in Fig. 14. Figures 14(a−c) show the rolling deformation characteristics of the samples in Route-A. The dislocation density gradient is formed in the direction perpendicular to the interface due to the effect of interface slip obstruction under low rolling deformation, while the interface starts to slip and relaxes the local large dislocation density when the rolling deformation is increased to 90%. The obstruction of interface to the Cu and 1010 steel slip is also observed in the samples in Route-B (Figs. 14(d) and (e)), and though the interface becomes rugged, its deformation is still significantly lower than that of free surface. The deformation and fracture occur mainly through slip for the two kinds of rolled samples, except for the 90%-rolling reduction samples that have lost enough plastic deformation capacity. The slip competition between Cu and 1010 steel leads to more complex fracture mechanisms of the Cu/1010 steel BLCs compared to monometallic material (Figs. 14(f−i)). Due to the slip obstruction effect of the interface, some dimples appear at the interface, suggesting that the interface acts as the origin of

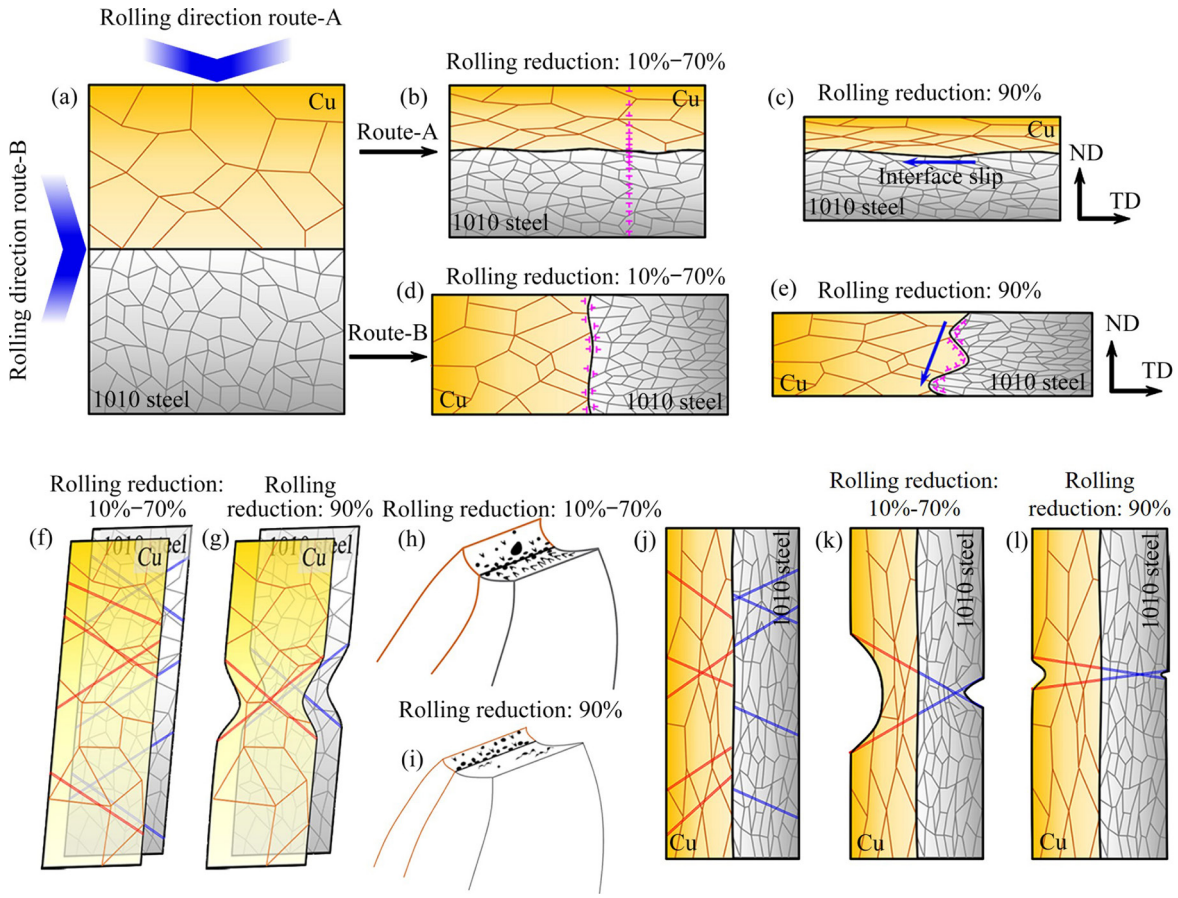

Fig. 14 Schematic diagrams of Cu/1010 steel BLCs microstructure evolution during rolling process: As-cast sample (a), Samples in Route-A (b, c) and Route-B (d, e); Deformation slips and necking process of Cu/1010 steel BLCs for samples in Route-A (f, g) and Route-B (j−l); Fracture surface schematic diagrams of samples in Route A (h, i)

cracks and induces the final fracture as seen in Figs. 14(h, i). The fracture process of the samples in Route-B shows that Cu suffers concentrated plastic deformation over a wider range than the 1010 steel in the necking region, as illustrated in Figs. 14(j−l).

5 Conclusions

(1) Cu has larger slip deformation capacity compared to the 1010 steel, leading to faster reduction in the thickness in Route-A. The percentage spread of Cu rises rapidly in Route-B, which in turn leads to the increase in cladding ratio. Some slip bands and textures also appear in the samples with larger rolling reductions.

(2) Strong texture is the main reason for the increase of strength, and due to the large volume fraction of the 1010 steel caused by lower cladding, the strength of samples in Route-A is larger than that in Route-B. Meanwhile, the plastic deformation behavior and fracture mechanisms of the samples exposed to different rolling directions and reduction variation due to different mechanical properties of the Cu and 1010 steel.

(3) Dislocation density gradient is formed under low rolling reductions due to the obstruction of the interface to crystal slip, and when the rolling reduction is increased to 90%, the interface starts to slip, leading to the disappearance of dislocations pile-up at the interface in Route-A. Due to different response of crystal planes to rolling loads, the slip planes have larger normal strain and lower shear strain after rolling in Route-B.

CRediT authorship contribution statement

Bo PENG: Conceptualization, Methodology, Investigation, Data Curation, Writing − Original draft; **Jia LIU:** Investigation; **Hui-kun WANG:** Investigation, Writing − Review & editing; **Xing-run SHAN:** Writing − Review & editing; **Guo-liang LI** and **Zi-di**

HANG: Investigation; **Jin-chuan JIE:** Funding acquisition, Supervision, Writing − Review & editing; **Ting-ju LI:** Funding acquisition, Supervision.

Declaration of competing interest

The authors declare that they have no known competing financial interests or personal relationships that could have appeared to influence the work reported in this paper.

Acknowledgments

The authors gratefully acknowledge the support from the National Key Research and Development Program of China (No. 2018YFE0306103), the National Natural Science Foundation of China (No. 52071050), the Science and Technology Innovation Project of Ningbo, China (No. 2021Z032), and the Program of China Scholarships Council (No. 202106060148).

References

[1] LI Zhou, ZHAO Jing-wei, JIA Fang-hui, LIANG Xiao-jun, ZHANG Qing-feng, YUAN Xiang-qian, JIAO Si-hai, JIANG Zheng-yi. Interfacial characteristics and mechanical properties of duplex stainless steel bimetal composite by heat treatment [J]. Materials Science and Engineering: A, 2020, 787: 139513.

[2] LIU Zhu-bo, WANG Xin-yue, LIU Ming-shuo, LIU Yuan-ming, LIU Jiang-lin, IGNATOV A V, WANG Tao. Microstructure and mechanical behavior of Ti/Cu/Ti laminated composites produced by corrugated and flat rolling [J]. Transactions of Nonferrous Metals Society of China, 2022, 32(8): 2598−2608.

[3] ZHANG Jian-yu, WANG Yan-hui, LÜ Zheng, CHEN Qing-an, CHEN Ya-yu, LI He-zong. Formation mechanism and growth kinetics of $TiAl_3$ phase in cold-rolled Ti/Al laminated composites during annealing [J]. Transactions of Nonferrous Metals Society of China, 2022, 32(2): 524−539.

[4] JIE Jin-chuan, LIU Cheng-bin, WANG Shi-hang, DONG Bo-wen, LIU Shi-chao, LI Ting-ju. Characterisation of steel/nickel bronze clad strips prepared by continuous solid/liquid bonding method [J]. Materials Science and Technology, 2019, 35(15): 1840−1847.

[5] LI Ting, WANG Tao, LIU Wen-wen, HUANG Zhi-quan, JIANG Zheng-yi, HUANG Qing-xue. Hot-rolling process and properties of large thickness ratio Al/Mg/Al laminates [J]. Transactions of Nonferrous Metals Society of China, 2023, 33(12): 3625−3640.

[6] DONG Bo-wen, JIE Jin-chuan, WANG Shi-hang, DONG Zhuang-zhuang, LI Ting-ju. Fabrication of Cu−24Pb−2Sn/C10 laminar composite by solid-liquid continuous casting compositing [J]. Materials Letters, 2020, 262(1): 127174.

[7] CHEN Chen, ZHOU Jian, XUE Feng, WU Qiu-ping. Elimination of liquid metal embrittlement cracks during arc cladding of tin bronze on steel sheet [J]. Materials Letters, 2020, 269: 127646.

[8] TAO X P, ZHANG S, ZHANG C H, WU C L, CHEN J, ABDULLAH O. Effect of Fe and Ni contents on microstructure and wear resistance of aluminum bronze coatings on 316 stainless steel by laser cladding [J]. Surface and Coatings Technology, 2018, 342: 76−84.

[9] WANG Yi-ran, GAO Yi-min, LI Ye-fei, ZHAI Wen-yan, ZHANG Chao. Review of preparation and application of copper−steel bimetal composites [J]. Emerging Materials Research, 2019, 8(4): 538−551.

[10] SABETGHADAM H, HANZAKI A Z, ARAEE A, HADIAN A. Microstructural evaluation of 410 SS/Cu diffusion-bonded joint [J]. Journal of Materials Science & Technology, 2010, 26(2): 163−169.

[11] GUO Miao, LI Sha, ZHAO Li-ping, HAN Jian-chao, WANG Tao. Effect of rolling temperature of corrugated roll on the interface structure and mechanical properties of Mg/Al composite plate [J]. Materials Review, 2020, 34(11B): 22087−22092.

[12] ZHOU Qiang, JIA Bin, GUO Bao-qiao, LIU Rui, ZHU Lei, BATAEV I A, CHEN Peng-wan. Microstructure and mechanical properties of the bonding interface of explosively welded TA2/Q235 composite under dynamic shear loading [J]. International Journal of Mechanical Sciences, 2022, 225(1): 107362.

[13] WANG Jun, ZHAO Fan, XIE Guo-liang, HOU Yu-fei, WANG Rui, LIU Xin-hua. Rolling deformation behaviour and interface evaluation of Cu−Al bimetallic composite plates fabricated by horizontal continuous composite casting [J]. Journal of Materials Processing Technology, 2021, 298: 117296.

[14] MENG L, ZHANG L, ZHOU S P, YANG F T. Effects of rolling and sintering temperature on peel strength of bonding interfaces for Ag/Cu bimetallic strips [J]. Materials Science and Technology, 2003, 19(6): 779−784.

[15] XU Jian-zhong, GAO Xing-jian, JIANG Zheng-yi, WEI Dong-bin, JIAO Si-hai. Microstructure and hot deformation behaviour of high-carbon steel/low-carbon steel bimetal prepared by centrifugal composite casting [J]. The International Journal of Advanced Manufacturing Technology, 2016, 86(1): 817−827.

[16] YANG Jun-fen, QU Kai, YANG Jing-lin. Fatigue performance of Q355B steel substrate treated by grit blasting with and without subsequent cold spraying with Al and Cu [J]. Surface and Coatings Technology, 2021, 405: 126662.

[17] HAN Xiu-zhu, HU Li, JIA Dong-yong, CHEN Jia-ming, ZHOU Tao, JIANG Shu-yong, TIAN Zheng. Role of unusual double-peak texture in significantly enhancing cold rolling formability of AZ31 magnesium alloy sheet [J]. Transactions of Nonferrous Metals Society of China, 2023, 33(8): 2351−2364.

[18] MAO Zhi-ping, XIE Jing-pei, WANG Ai-qin, WANG Wen-yan, LI Yan, MA Dou-qin. Interfacial microstructure and bonding strength of copper/aluminum clad sheets produced by horizontal twin-roll casting and annealing [J].

Materials Research Express, 2019, 6(1): 016505.

[19] LIU Wen-zheng, WANG Dong-ya, CAO Xiao-qing, WANG Li-fei, WANG Wen-xian. Numerical simulation of the rolling process for Mg/Al explosive welding composite plate with thermo-mechanical coupled model [J]. Forging & Stamping Technolog, 2016, 41(10): 166−170.

[20] LEE S B, LEDONNE J E, LIM S C V, BEYERLEIN I J, ROLLETT A D. The heterophase interface character distribution of physical vapor-deposited and accumulative roll-bonded Cu−Nb multilayer composites [J]. Acta Materialia, 2012, 60(4): 1747−1761.

[21] HOSEINI-ATHAR M M, TOLAMINEJAD B. Interface morphology and mechanical properties of Al−Cu−Al laminated composites fabricated by explosive welding and subsequent rolling process [J]. Metals and Materials International, 2016, 22(4): 670−680.

[22] JIANG Lian-yun, CHEN Ya-fei, LIANG Jia-le, LI Zhen-lei, WANG Tao, MA Li-feng. Modeling of layer thickness and strain for the two-layered metal clad plate rolling with the different roll diameters [J]. Journal of Materials Research and Technology, 2024, 28: 3849−3864.

[23] LI Zhen-lun, SONG Ke, KANG Qing-xin, ZHOU Tong-xv, XV Xun-hu, ZHAN Li-qiang, WANG Guo-feng. Microstructure evolution during high temperature rolling and effect on the mechanical properties of TiB_w/Ti65 composites with network structure [J]. Materials Characterization, 2024, 208: 113642.

[24] CAI Yuan, SUN Huan-teng, CAI Qing-shan, LIU Wen-sheng, MA Yun-zhu, DUAN You-teng. Effect of hot rolling on microstructure and mechanical properties of hot isostatically pressed 30CrMnSiNi2A ultrahigh strength steel [J]. Materials Science and Engineering: A, 2024, 891: 145956.

[25] SUWAS S, SINGH A K, RAO K N, SINGH T. Effect of modes of rolling on evolution of the texture in pure copper and some copper-base alloys Part I: Rolling texture [J]. Zeitschrift für Metallkunde, 2002, 93(9): 918−927.

[26] LI Sheng-ci, GUO Cheng-yu, HAO Lei-lei, KANG Yong-lin, AN Yu-guo. In-situ EBSD study of deformation behaviour of 600 MPa grade dual phase steel during uniaxial tensile tests [J]. Materials Science and Engineering: A, 2019, 759: 624−632.

[27] LIU Ya-hui, LIU Shi-feng, DENG Chao, FAN Hai-yang, YUAN Xiao-li, LIU Qing. Inhomogeneous deformation of $\{111\}\langle uvw\rangle$ grain in cold rolled tantalum [J]. Journal of Materials Science & Technology, 2018, 34(11): 2178−2182.

[28] SHAYANPOOR A A, REZAEI A H. Constitutive model for hot deformation behaviors of Al/Cu bimetal composites based on their components [J]. Transactions of Nonferrous Metals Society of China, 2023, 33(12): 3641−3660.

[29] NI Xin-bo, LIU Zhuang-zhuang, MIAO Ke-song, LENG Jin-feng, FAN Guo-hua, TENG Xin-ying, WU Hao. Interfacial-constraint-induced intragranular deformation inhomogeneity of Ti−Al layered composites [J]. Transactions of Nonferrous Metals Society of China, 2023, 33(3): 789−801.

[30] WANG Chun-yang, JIANG Yan-bin, XIE Jian-xin, XU Sheng, ZHOU De-jing, ZHANG Xiao-jun. Formation mechanism and control of aluminum layer thickness fluctuation in embedded aluminum–steel composite sheet produced by cold roll bonding process [J]. Transactions of Nonferrous Metals Society of China, 2017, 27(5): 1011−1018.

[31] CARPENTER J S, VOGEL S C, LEDONNE J E, HAMMON D L, BEYERLEIN I J, MARA N A. Bulk texture evolution of Cu−Nb nanolamellar composites during accumulative roll bonding [J]. Acta Materialia, 2012, 60(4): 1576−1586.

[32] LIU Shuai-yang, WANG Ai-qin, LIANG Ting-ting, XIE Jing-pei. Hot deformation behavior of Cu/Al laminated composites under interface constraint effect [J]. Materials Research Express, 2018, 5(6): 066531.

[33] WANG Chen, MA Li-nan, MA Xiao-guang, WANG Tao, JIANG Zheng-yi, HASAN M, ZHAO Jing-wei. Effect of annealing temperature on microstructure and tensile properties of copper/aluminum composite thin strip [J]. Transactions of Nonferrous Metals Society of China, 2023, 33(3): 701−713.

[34] WANG De-zhi, JI Yao-xin, WU Zhuang-zhi. Effects of cross rolling on texture, mechanical properties and anisotropy of pure Mo plates [J]. Transactions of Nonferrous Metals Society of China, 2020, 30(8): 2170−2176.

[35] ZHI Chen-chen, WU Zhen-yu, MA Li-feng, HUANG Zhi-quan, ZHENG Ze-bang, XV Hai-jie, JIA Wei-tao, LEI Jun-yi. Effect of thickness ratio on interfacial structure and mechanical properties of Mg/Al composite plates in differential temperature asymmetrical rolling [J]. Journal of Materials Research and Technology, 2023, 24: 8332−8347.

[36] PENG Bo, JIE Jin-chuan, WANG Ming-fei, DONG Bo-wen, WANG Xian-long, LI Shun-yu, LI Ting-ju. Microstructure characteristics and deformation behavior of tin bronze/1010 steel bimetal layered composite by continuous solid/liquid bonding [J]. Materials Science and Engineering: A, 2022, 844: 143155.

[37] PENG Bo, HANG Zi-di, JIE Jin-chuan, LOU Shu-min, WANG Hui-kun, MURAISHI S, LI Ting-ju. Evolution of interface and mechanical performance of Cu−xAl/1010 steel bimetal laminated composite [J]. Journal of Alloys and Compounds, 2023, 935: 168121.

[38] HŸTCH M J, SNOECK E, KILAAS R. Quantitative measurement of displacement and strain fields from HREM micrographs [J]. Ultramicroscopy, 1998, 74(3): 131−146.

[39] PENG Bo, JIE Jin-chuan, LIU Jia, QU Jian-ping, WANG Ming-fei, SUN Jia, CHEN Xiao-hu, REN Zheng, LI Ting-ju. Synergetic strengthening of heterogeneous interface far beyond rule of mixture in Cu/1010 steel bimetal laminar composite [J]. Materials Science and Engineering: A, 2022, 851: 143609.

[40] LEMARQUIS L, GIROUX P F, MASKROT H, CASTANY P. Activated twinning variant determination in cold-rolled 316L stainless steel by effective Schmid factor analysis [J]. Materialia, 2023, 30: 101812.

[41] NOELL P J, CARROLL J D, BOYCE B L. The mechanisms of ductile rupture [J]. Acta Materialia, 2018, 161: 83−98.

[42] TIAN Yu-he, LUO Nian-chun, HE Wei-jun, JIANG Bin, PAN Fu-sheng. Effect of Zn and Ti transition foil on the microstructure and mechanical properties of hot rolling

bonded Al/Mg composite plates [J]. Materials Science and Engineering: A, 2024, 891: 145978.

[43] LIU X Y, CAPOLUNGO L, HUNTER A. Screw dislocation impingement and slip transfer at fcc−bcc semicoherent interfaces [J]. Scripta Materialia, 2021, 201: 113977.

[44] WANG C J, YAO B N, LIU Z R, KONG X F, LEGUT D, ZHANG R F, DENG Y. Effects of solutes on dislocation nucleation and interface sliding of bimetal semi-coherent interface [J]. International Journal of Plasticity, 2020, 131: 102725.

轧制方向和压下量对铜/1010 钢双金属复层材料显微组织演变及力学性能的影响

彭 博[1]，刘 佳[1]，王会琨[1]，单星润[1]，李国梁[1]，杭子迪[1]，接金川[1,2]，李廷举[1,2]

1. 大连理工大学 材料科学与工程学院 辽宁省凝固控制与数字化制备技术重点实验室，大连 116024；
2. 大连理工大学 宁波研究院，宁波 315000

摘 要：将铜/1010 钢的双金属复层材料轧制成不同厚度以研究轧制方向和压下量对其显微组织演变及力学性能的影响。铜与 1010 钢间力学性能的差异导致产生了不同厚度减少量、宽展率和包覆率。强织构的形成同时增大了轧制样品的强度，并且由于路线 A 样品中 1010 钢的体积分数较大，其强度始终高于路线 B 中样品的强度。界面对晶体和位错滑移的阻碍作用导致界面畸变的形成，并导致压下量较低时路线 A 中界面附近出现位错密度梯度。在轧制载荷的作用下，界面附近 Cu 和 1010 钢的滑移面更倾向于产生正应变，而其他晶面的剪切应变则明显大于正应变。

关键词：铜/钢双金属复层材料；轧制；显微组织演变；力学性能；变形行为

(Edited by Wei-ping CHEN)